



Construction of CeO₂/CdS Heterostructure and Study on Photocatalytic Mechanism of Rhodamine B Degradation

Ziwei Liu¹ · Yanli Zhuang¹ · Limin Dong¹ · Hongxu Mu¹ · Dan Li¹ · Leiming Wang¹ · Shuo Tian¹

Received: 5 June 2023 / Accepted: 26 July 2023 / Published online: 5 August 2023

© The Author(s), under exclusive licence to Springer Science+Business Media, LLC, part of Springer Nature 2023

Abstract

A series of CeO₂/CdS photocatalysts were prepared by simple solvothermal and auxiliary calcination using cerium nitrate as the precursor. Two different forms of CeO₂ (nanosheets (NF-CeO₂) and nanorods (NR-CeO₂)) were successfully prepared and used to degrade rhodamine B (RhB) to study the photocatalytic activity of the composites. On this basis, the effects of composite proportion and preparation technology on the photocatalytic activity of the composites were studied. The morphology, structure, photoelectric properties and chemical composition of the composites were analyzed. Compared with single photocatalysts (NR-CeO₂ and CdS), the NF-CeO₂/CdS and NR-CeO₂/CdS composite catalyst have stronger photocatalytic performance. In addition, capture experiments and ESR showed that both •O₂⁻ and h⁺ impacted on the RhB degradation. After four repeated cycles, NR-CeO₂/CdS (1:6) showed stable RhB degradation activity. In the aspect of catalyst interface design, this work not only provides an effective method for the preparation of catalysts with high photodegradation rate and good reuse, but also provides a feasible idea for further research on the degradation of emerging pollutants by photocatalysts.

Keywords CeO₂/CdS photocatalysts · Morphology control · RhB degradation · Type II heterojunction structure · Photocatalytic mechanism

1 Introduction

As a consequence of economic development, population growth and the industrial development brought environmental pollution and energy crises to the ecosystem, which have caused serious environmental problems and threaten the health of human and the sustainable development of economics [1–3]. The major pollutant is water pollution, it a critical social issue because water quality is closely related to our day-to-day living. Therefore, finding an effective method to remove the emerging recalcitrant organic pollutants from wastewater is extremely necessary. In photocatalysis process, photocatalyst has a greatly influence to the photocatalytic degradation efficiency of pollutants. Thus, the search for excellent photocatalysts will never stop. Among

various photocatalysts, semiconductor nanomaterials have received more attentions due to the merits of low cost and high activity, which is one of the promising green energy technologies and plays an important role in environmental pollutants degradation, such as ZnO, TiO₂, and g-C₃N₄ [4–6]. Unfortunately, the applications of these traditional photocatalysts are generally limited due to their inherent wide band gap and low degradation efficiency [7–9]. The abundant rare earth oxides, as a new type of semiconductor photocatalyst, which has attracted utilized based on its superior photocatalytic properties under visible light irradiation due to its appropriate band gap and energy band positions [10, 11]. As one of the most abundant, cerium dioxide (CeO₂) has a favorable application prospects due to its strong oxygen storage capacity, low cost, non-toxicity, easy conversion from Ce⁴⁺ to Ce³⁺ and chemically and biologically stable [12–14]. However, wide band gap (about 2.7 eV), rapid recombination of electron–hole, and lower visible light utilization efficiency (about 4% of solar energy) restrict CeO₂'s photocatalytic ability. To overcome the above-mentioned issues, CeO₂-based composites have been widely designed to improve its photocatalytic degradation of organic pollutants. Such as element doping, formation

✉ Yanli Zhuang
zhuangyanli@hrbust.edu.cn

¹ Heilongjiang Provincial Key Laboratory of CO₂ Resource Utilization and Energy Catalytic Materials, School of Material Science and Chemical Engineering, Harbin University of Science and Technology, Harbin 150040, China

the type II and Z-scheme heterojunction structure with other semiconductors, manufacturing defects, etc. [15–18]. Among them, many CeO₂-based composites based on type II and Z-scheme heterostructures to increase the migration rate of photogenerated charge carriers and the light utilization efficiency of photocatalytic materials, which exhibit better visible light absorption photocatalytic performance than CeO₂ alone [19, 20]. For instance, Zhang et al. have successfully used the one-step co-precipitation method to synthesize CeO₂ on the surface of BiOI. The CeO₂/BiOI heterostructure exhibited good photodegradation property for RhB under visible light irradiation, which reached 98% in 60 min [21].

Cadmium sulfide (CdS), considered as one of the most promising material for photocatalytic material due to the suitable bandgap, excellent visible light absorption and excellent capacity for charge carrier transport [22, 23]. More importantly, CdS can form heterojunction structure with CeO₂ due to its appropriate matched bandgap, thus effectively improving the photocatalytic activity of CeO₂ [24–26]. It has been reported that the microstructure of materials, including band structure and electron transfer process, is greatly affected by its tunable morphology [27]. Up to now, many morphologies of CeO₂ and CdS have been synthesized, such as 1D CdS nanorods and 2D CeO₂ nanosheets into composites, the composite showed better photocatalytic degradation ability, and the decomposition rate of tetracycline removal was up to 98.0% [28]. And 1D CdS nanoparticles/1D CeO₂ nanoparticles into composites, which has good photocatalytic degradation efficiency, and the degradation rate of pollutants reaches about 76.0% after 120 min with simulated sunlight [29]. Therefore, the microstructure of the composite can be further improved via adjust the morphology, including charge transfer efficiency and band structure, which is conducive to the construction of heterojunction and the improvement of photocatalytic performance.

In this paper, a series of CeO₂/CdS photocatalysts were prepared using cerium nitrate as precursor by a facile solvothermal method and assisted calcination method. 1D CdS nanorods were successfully fixed on 2D NF-CeO₂ and 3D NR-CeO₂. As previously reported heterojunction formed between CdS and CeO₂ can greatly inhibit the recombination of photogenerated charge carriers, CdS/CeO₂ shows excellent RhB degradation performance under light irradiation. The experimental results showed that the composited effect of NR-CeO₂/CdS was better compared with NF-CeO₂/CdS, and the degradation efficiency was up to 98.3%, which was much higher than that of CdS and NR-CeO₂. The visible light catalytic performance of CeO₂ was investigated by degrading RhB. When used in combination with CdS nanoparticles, it can be significantly enhanced. This excellent activity is mainly attributed to the high energy crystal

surface exposure of CeO₂, which greatly promotes the separation of electron–hole pairs [30]. In addition, through transmission electron microscopy high resolution transmission electron microscopy (TEM) high resolution transmission electron microscopy (HRTEM) characterization analysis, it was found that the surface differences of the main exposed crystals and the effect of morphology on the surface atomic structure of the crystals [31–34]. The type II transfer mechanism of NR-CeO₂/CdS composites was verified by capture experiments and ESR technique.

2 Experimental Section

2.1 Materials

Cerium nitrate hexahydrate (Ce(NO₃)₃·6H₂O), ammonium bicarbonate (NH₄HCO₃), sodium hydroxide (NaOH), cadmium nitrate tetrahydrate (Cd(NO₃)₃·5H₂O), thiourea (CH₄N₂S), barium sulfate (BaSO₄), benzoquinone (BQ), p-benzoquinone (IPA), Sodium oxalate (Na₂C₂O₄), RhB were purchased from McLean (Shanghai, China). Deionized water, Dimethyl Formamide (DMF) and methanol were provided by Yongchang chemical reagent.

2.2 Preparation Method

2.2.1 Preparation of NF-CeO₂

1.39 g Ce(NO₃)₃·6H₂O was dissolved in 200 mL deionized water with the aid of magnetic stirring. Then, 0.75 g NH₄HCO₃ was dissolved in 200 mL with the aid of magnetic stirring. When transparent solution was obtained, Aqueous solution of NH₄HCO₃ was further added into the Ce(NO₃)₃·6H₂O solution and magnetically stirred for 30 min to form a uniform suspension at 0 °C temperature. Then the sediment collected through filtering, centrifuge with deionized water. All of the obtained precursors were calcined at 400 °C for 4 h, and cooled at room temperature. The procedure of preparing is appeared in Scheme 1.

2.2.2 Preparation of NR-CeO₂

0.87 g Ce(NO₃)₃·6H₂O was dissolved in 20 mL deionized water with the aid of magnetic stirring. When transparent solution was obtained, quickly adding 10 mL of 1 mol/L sodium hydroxide solution with the aid of magnetic stirring for another 5 min at room temperature. Subsequently, the suspension was transferred into Teflon lined stainless steel autoclave, which was then heated at 130 °C for 18 h. The procedure of preparing is appeared in Scheme 2.

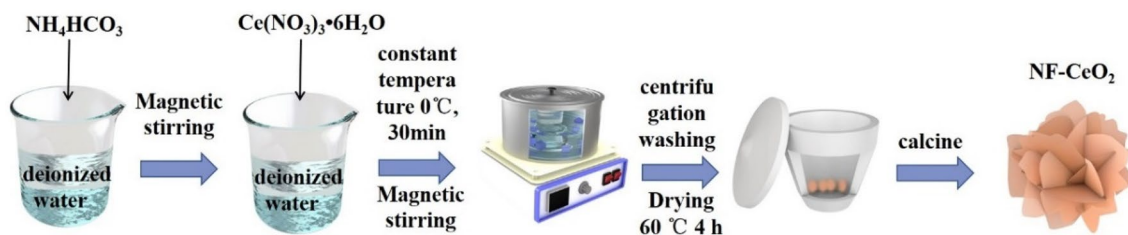
2.2.3 Synthesis of CeO₂/CdS

0.274 g of Cd(NO₃)₂·4H₂O and 0.05 g CH₄N₂S were dispersed into 35 mL of DMF, The mixture was sonicated for 20 min, to which the prepared NF-CeO₂ or NR-CeO₂ was further added. Magnetic stir after 5 min and transferred to a Teflonlined stainless steel autoclave with 100 mL capacity. Hydrothermal synthesis was then conducted at 200 °C for 3 h in an electric oven. After the reaction, the products were washed thoroughly with DMF and methanol and dried for a further 12 h at 60 °C to get the final products. The synthesis process are shown in Scheme 3 and Scheme 4.

2.3 Material Characterization

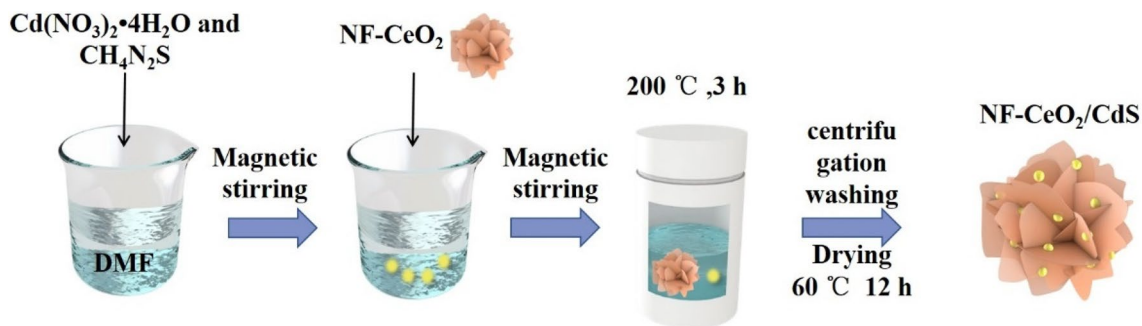
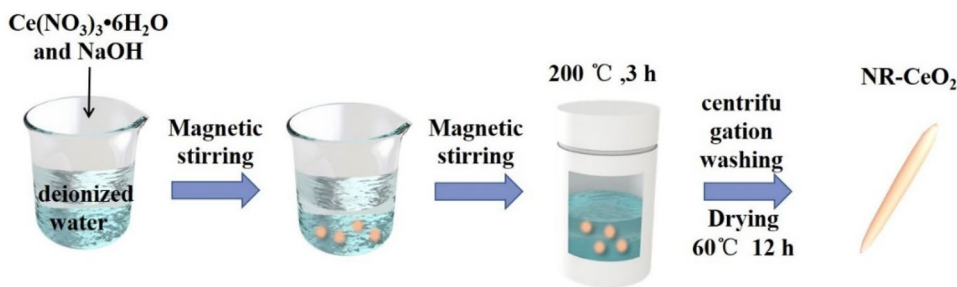
The crystal structure of the powder samples was investigated with X-ray diffraction (XRD, Model D/MAX-3b) with

Cu-Kα radiation ($\lambda = 0.154$ nm), using a voltage of 40 kV, a current of 10 mA, in 2θ ranges from 5° to 80°. The morphology of the samples were studied by field-emission scanning electron microscopy (SEM, FEI Sirion200), at an accelerating voltage of 20 kV with an energy-dispersive X-ray spectrometer (EDS), and the crystal structure and lattice spacing of samples were featured by transmission electron microscopy (TEM, JEM2100) at an accelerating voltage of 200 kV. X-ray photoelectron spectroscopy (XPS, Thermo Escalab 250Xi) was used at 15 kV voltage to characterize the chemical states of the powder samples. UV–vis diffuse reflectance spectra (UV-DRS, UV-757CRT) were measured at room temperature by mixing samples with BaSO₄ powder, and using it as the reference substance for reflectivity. The photoluminescence (PL) spectra of samples collected on shimadzu RF-5301 spectrophotometer were used to determine the recombination of electrons and holes in

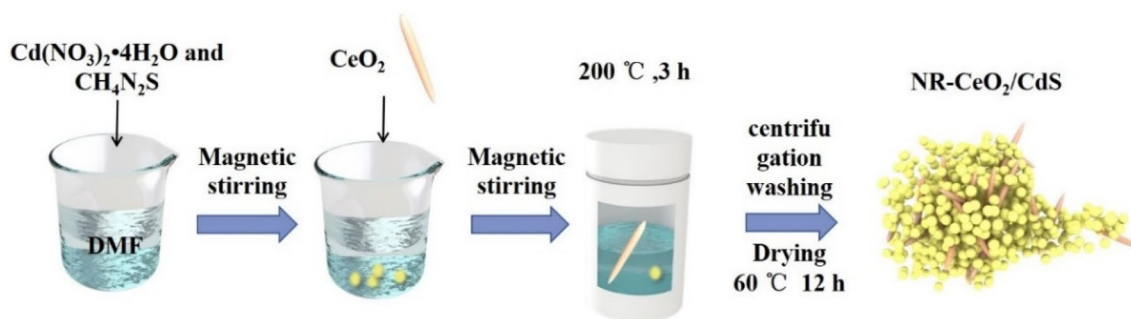


Scheme 1 Flow chart of NF-CeO₂ preparation

Scheme 2 Flow chart of NR-CeO₂ preparation



Scheme 3 Schematic diagram of material preparation: synthesis of the NF-CeO₂/CdS



Scheme 4 Schematic diagram of material preparation: synthesis of the NR-CeO₂/CdS

the photocatalyst. The excitation wavelength was 280 nm. Photocurrent response (I-T), Mott–Schottky (MS) measurements, Electrochemical impedance spectra (EIS), linear sweep voltammetry (LSV) were carried out on VMP3 electrochemical workstation to study the FTO working electrode. The saturated Ag/AgCl and Platinum electrodes are the counter electrode and the reference electrode respectively, and 0.5 M Na₂SO₄ is the electrolyte.

2.4 Photocatalytic Experiment

The photocatalytic activity of CeO₂/CdS catalysts were determined by the decomposition of RhB under visible light illumination. Briefly, 50 mg of sample was mixed with 50 ml of RhB solution (20 mg/L) and continuously stirred in a beaker for 3 h. Under dark condition, Stirred on the beaker for 1 h to obtain the adsorption–desorption equilibrium. After that, the suspension was continuously irradiated with a 300 W xenon lamp (GX2500, Shanghai). About 6 ml of liquid was taken from the beaker every 0.5 h for centrifugation, and the supernatant was taken for analysis by visible spectrophotometer. The adsorption wavelength of RhB used was 450 nm. In addition, 1 mmol BQ, 1 mmol IPA, and 1 mmol Na₂C₂O₄ were used as scavengers of ·O²⁻, ·OH, and h⁺, respectively. Electron spin resonance (ESR, EMX-500

10/12) spectra was performed to detect the reactive species, including 5, 5-dimethyl-1-pyrroline N-oxide (DMPO) capture radical ·O²⁻ and 2,2,6,6-Tetramethylpiperidinoxy (TEMPO) capture radical h⁺.

3 Results and Discussion

3.1 XRD phase Analysis

The crystallographic and phase structure of the obtained samples were examined by XRD, and the diffraction patterns were shown in Fig. 1. As shown in Fig. 1a, all the diffraction peaks were exactly matched to cubic phase CeO₂ for pure CeO₂ (JCPDS No. 34–0394), while the characteristic peaks of CdS can be indexed to the hexagon phase CdS (JCPDS No. 41-1049). No other impurity peaks were found, indicating that high purity CeO₂ and CdS were prepared, and the peak of NR-CeO₂ was sharper than that of NF-CeO₂. No other impurity peaks were found in the XRD pattern, indicating high purity of the material. The main diffraction peaks of CeO₂ in 2θ value of 23.89°, 30.25°, 32.72°, 42.30°, 46.97°, 56.89° belong to the (011), (013), (110), (114), (020), (123) crystal planes of the tetragonal CeO₂ (JCPDS No. 34-0394), respectively. Furthermore, the diffraction data of CdS, the

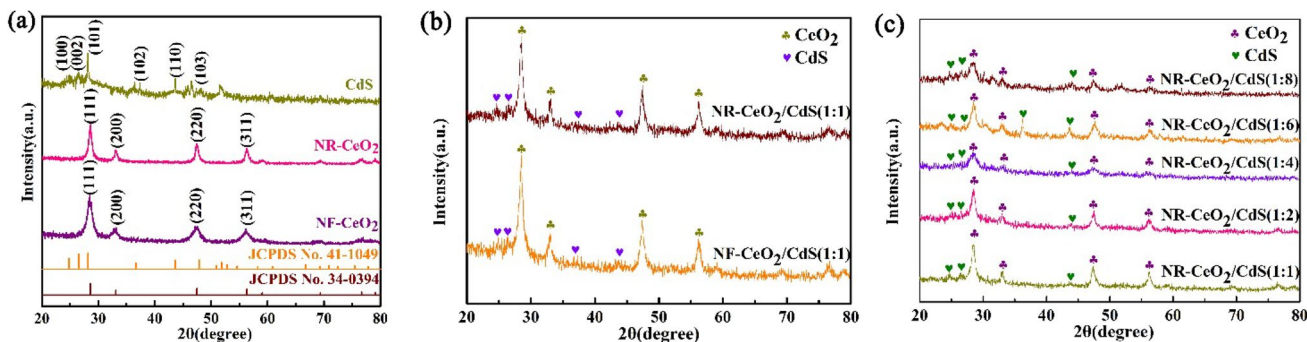


Fig. 1 XRD patterns of CeO₂ with different morphologies and CdS

main diffraction peaks at 2θ value of 24.81° , 26.51° , 28.18° , 36.62° , 43.68° , and 47.84° belong to the (100), (002), (101), (110), (102), (110), and (103) crystal planes of the hexagon phase CdS (JCPDS No. 41-1049), respectively. As shown in Fig. 1b, the XRD data exhibited composite characteristics after the addition of CeO_2 for the CdS, and compared with NF- CeO_2/CdS , the diffraction peaks of CdS and CeO_2 are sharper indicates that NR- CeO_2/CdS possessed better crystallinity. It is note-worthy that some characteristic peaks of CeO_2 (JPCDS No. 34-0394) also appeared in the XRD diffraction pattern, indicating the successful combing of CeO_2 in the composite. Meanwhile, the XRD patterns in Fig. 1c exhibited the main diffraction peaks of CdS (marked with the symbol of ♣) and CeO_2 (marked with the symbol of ♥). What's more, the NR- CeO_2/CdS indicated that when the amount of NR- CeO_2 increased, the intensities of characteristic peaks raised consequently. Compared with CdS, there is no significant difference in XRD, proving that the presence of CdS negligibly influenced the crystal morphology of NR- CeO_2 . On the other hand, the peak intensity in the diffraction pattern is lower or the peak width is wider than that of the pure material. It also indicates that NR- CeO_2 interacts

with CdS to some extent. In summary, NR- CeO_2/CdS was successfully prepared based on the XRD diffraction pattern.

3.2 The Microstructure of the Photocatalysts

The morphology characteristics investigated by SEM are shown in Figs. 2, 3, 4 and 5. The pure NF- CeO_2 sample (Fig. 2a) consists of a large number of 2D nanosheets interwoven and assembled into a 3D flower structure, while NR- CeO_2 (Fig. 2b) has a bar structure with a length of about $1\ \mu\text{m}$. CdS (Fig. 2c) consists of unregular spherical particles. After loading NF- CeO_2 , the morphology of CdS has been largely maintained, many nanoparticles are also noticed on the surface layer (in Fig. 3a). In Fig. 3b, after loading NR- CeO_2 , nanorods were also observed interspersed among the agglomerated nanoparticles. This indicates that CeO_2 and CdS coexist in CeO_2/CdS composites. The composites of NR- CeO_2/CdS possess the highest photocatalytic performance among all samples (to be investigated in later photocatalytic test), so the detailed studies are focused on NR- CeO_2/CdS . Notably, the distribution of NR- CeO_2 on the CdS nanoparticles surface

Fig. 2 SEM images of **a** NF- CeO_2 ; **b** NR- CeO_2 ; and **c** CdS

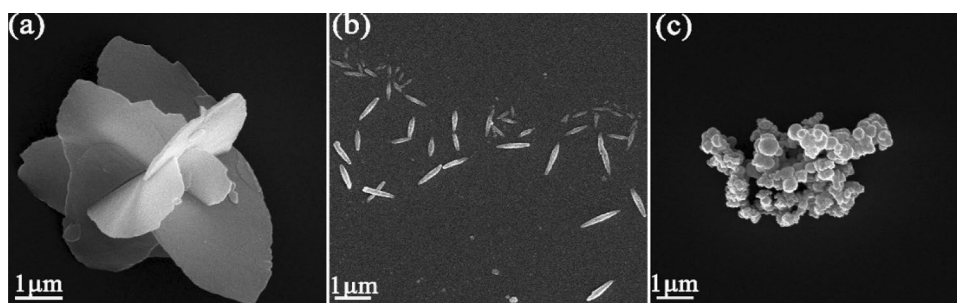
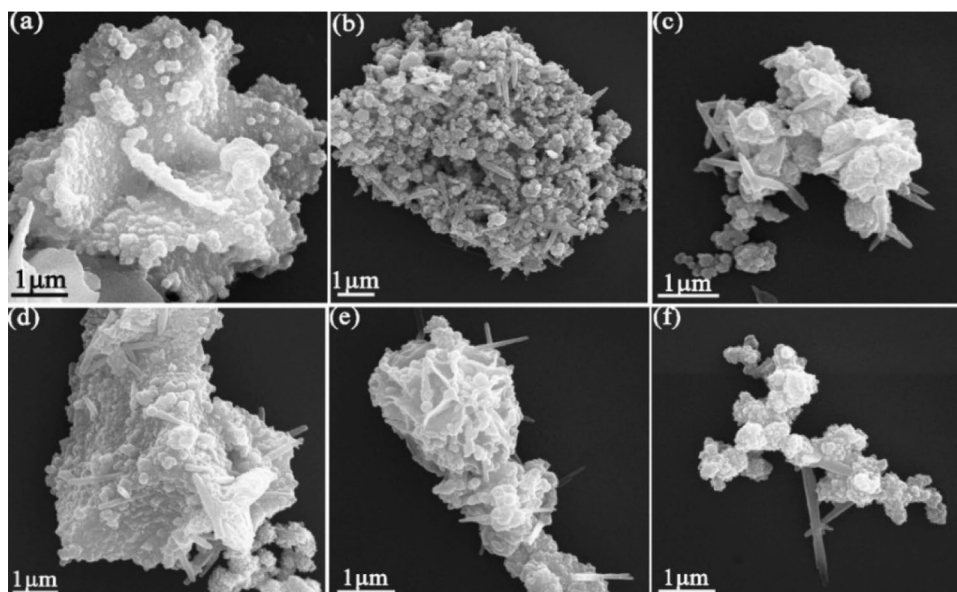


Fig. 3 SEM images of the samples prepared with different mass ratios. **a** NF- CeO_2/CdS (1:1); **b** NR- CeO_2/CdS (1:1); **c** NR- CeO_2/CdS (1:2); **d** NR- CeO_2/CdS (1:4); **e** NR- CeO_2/CdS (1:6); **f** NR- CeO_2/CdS (1:8)



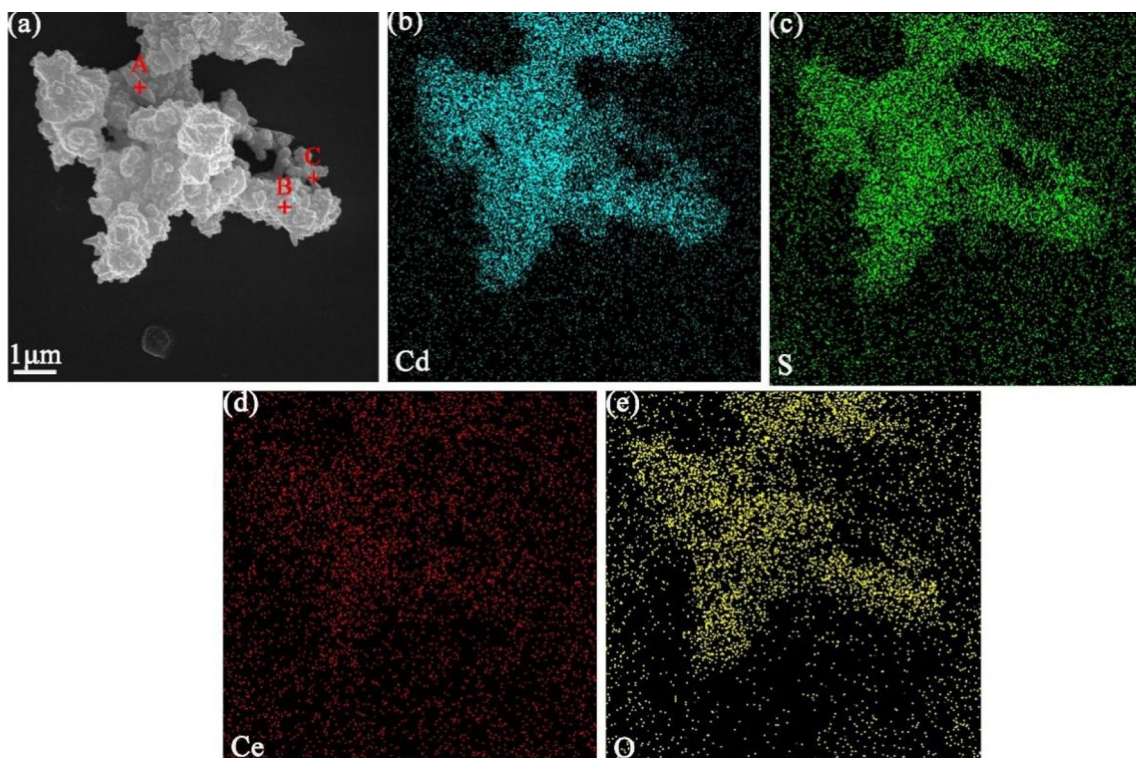


Fig. 4 Elements maps analysis of NR-CeO₂/CdS: **a** EDS patterns; **b–e** element analysis of Cd, S, Ce and O

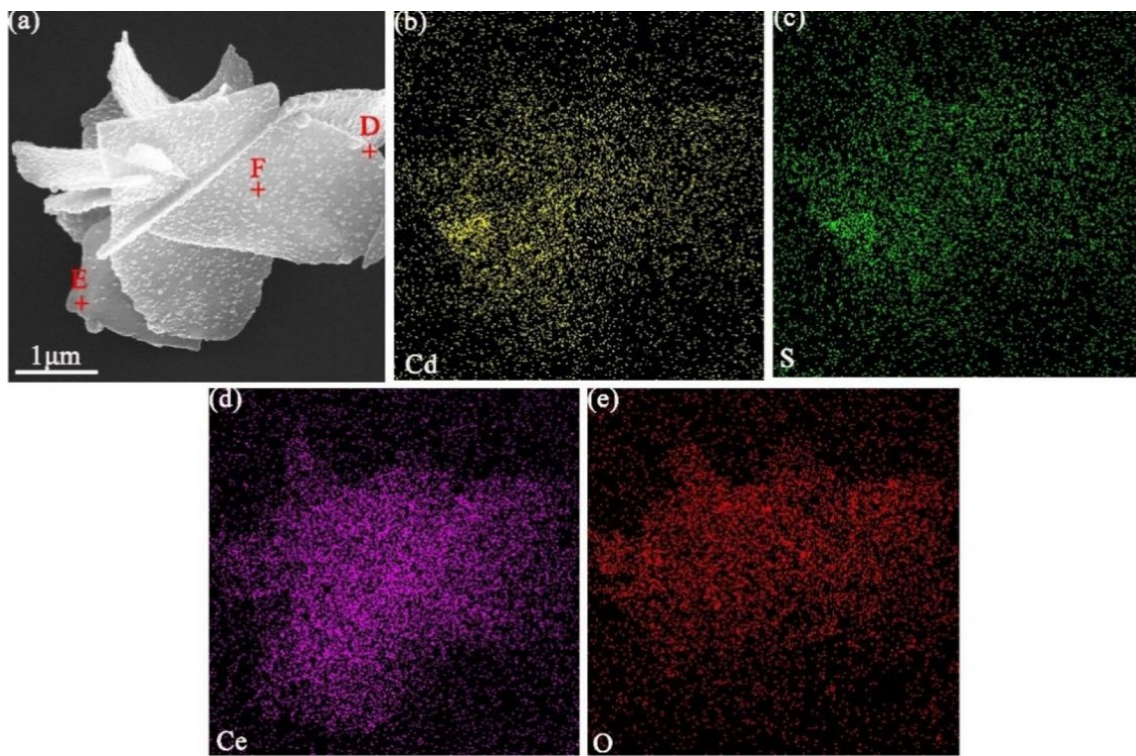


Fig. 5 Elements maps analysis of NF-CeO₂/CdS: **a** EDS patterns; **b–e** element analysis of Cd, S, Ce and O

Table 1 The EDS consequences of the points signed in Fig. 10a

Position	Composition (wt. %)				Possible substance
	Cd	S	Ce	O	
A	0	0	50.96	49.04	CeO ₂
B	85.93	14.07	0	0	CdS
C	71.12	15.69	5.83	7.36	CeO ₂ /CdS

Table 2 The EDS consequences of the points signed in Fig. 11a

Position	Composition (wt. %)				Possible substance
	Cd	S	Ce	O	
D	0	0	86.42	13.58	CeO ₂
E	82.26	17.74	0	0	CdS
F	16.92	3.41	52.28	27.39	CeO ₂ /CdS

is decreased with reducing the content of NR-CeO₂ in the Fig. 3b–f. Figure 4 and Fig. 5 are element maps of NF-CeO₂/CdS (1:1) and NR-CeO₂/CdS (1:1), respectively. The corresponding EDS results helped to confirm homogeneous elemental distribution and chemical composition of all samples. It can be seen that the elemental distribution of Ce is sparse, owing to the fact that the content of Ce is lower than Cd, S and O. Meanwhile, the Tables 1 and 2 also confirm that all elements (Cd, S, Ce and O) distributed in the composite, elucidating that CeO₂/CdS composites were formed.

3.3 Transmission Electron Microscopy Analysis

Figure 6 exhibits the TEM images of NR-CeO₂/CdS and NF-CeO₂/CdS. As shown in Fig. 6a and d, NR-CeO₂ has an obvious rod-like structure, NF-CeO₂ has a flower-like structure, and CdS has a granular structure, which is consistent with SEM results. From Fig. 6b, e and f, it can be found that the composite has some irregular particles on CeO₂ surface, which matches well with SEM results. As shown in Fig. 6c and g, different lattice fringes were found in HRTEM images of pure CeO₂, belonging to (311) and (220) crystal planes respectively, with d-spacing of 0.167 and 0.210 nm, respectively. The interplanar spacings of 0.187 nm can be indexed to CdS planes. The smooth lattice connection between CdS and CeO₂ as shown in Fig. 3d and g demonstrates the successful combined of CeO₂ onto CdS. Different exposed crystal planes may be one of the main reasons for different photocatalytic performance.

3.4 XPS Analysis

In order to further analyze the chemical composition and surface electronic states of NR-CeO₂/CdS, XPS test was carried out. As shown in Fig. 7a, the exist of Cd, S, Ce and O elements in NR-CeO₂/CdS was confirmed in the full-scan spectrum. The high-resolution spectra of Cd 3d, S 2p, Ce 3d and O 1s are presented in Fig. 7b–e, respectively. Figure 7b illustrated the high-resolution spectrum of Cd 3d, which presented two strong peaks at 405.2 and 411.9 eV, belonging to Cd 3d_{5/2}

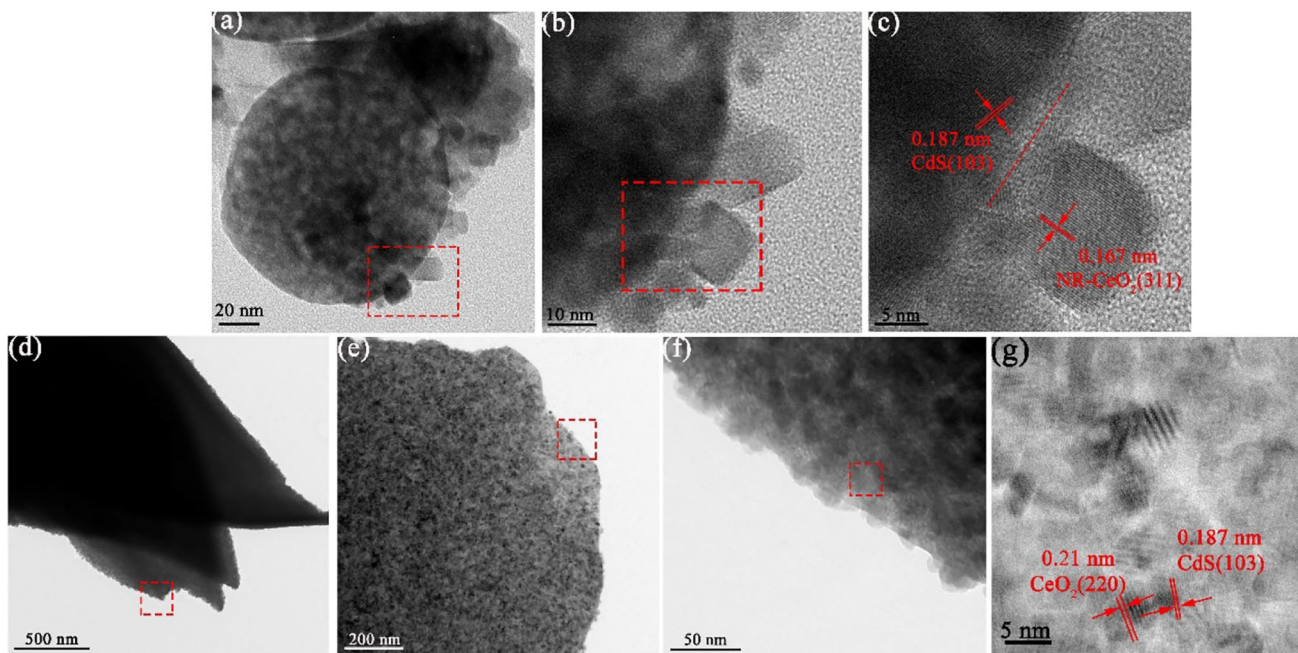


Fig. 6 TEM images of NR-CeO₂/CdS (a and b); HRTEM image of NR-CeO₂/CdS (c); TEM images of NF-CeO₂/CdS (d–f); HRTEM image of NF-CeO₂/CdS (g)

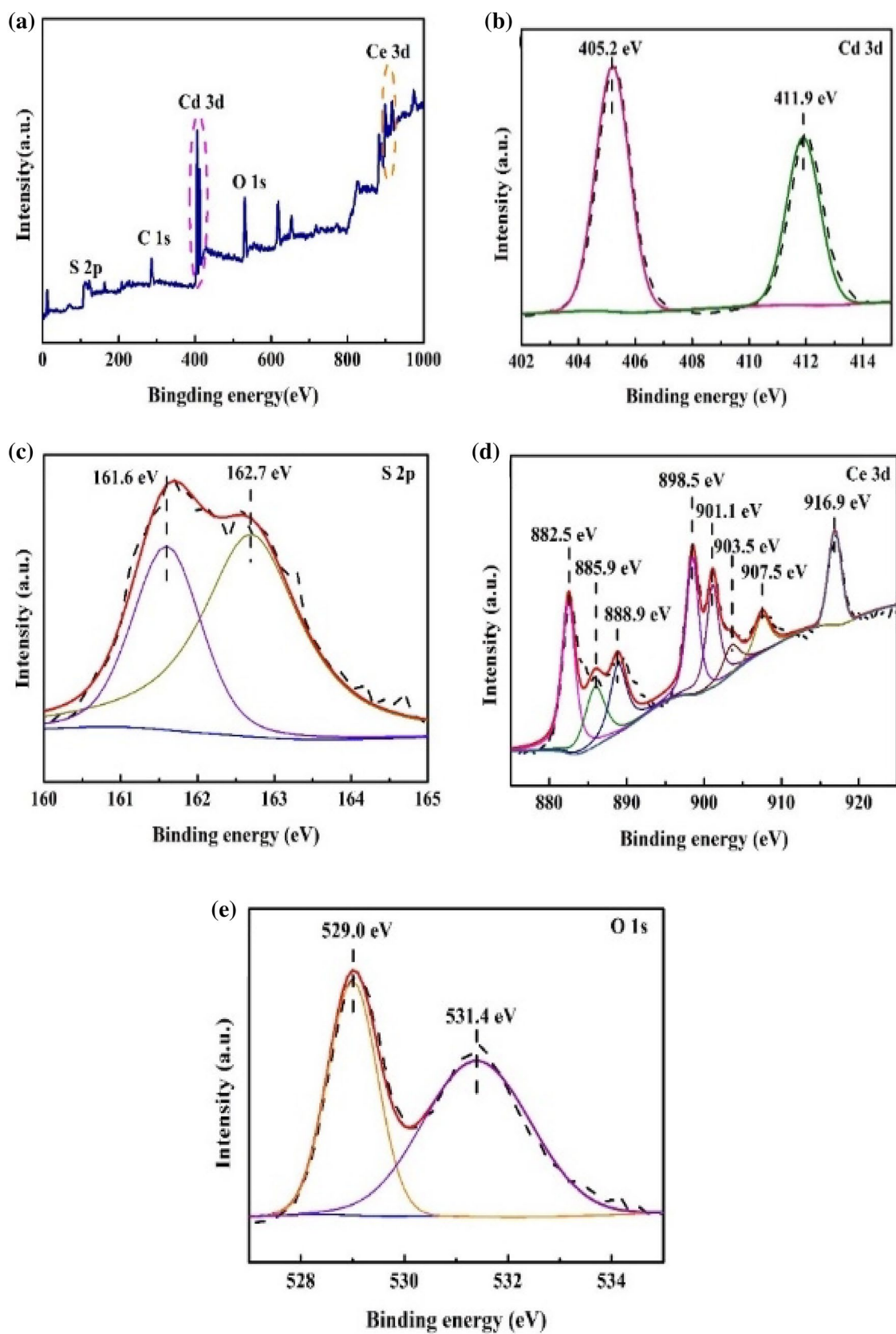


Fig. 7 The XPS spectra of NR-CeO₂/CdS: **a** survey scan, **b** Cd 3d spectra, **c** S 2p spectra, **d** Ce 3d spectra **e** O 1s spectra

and $3d_{3/2}$, these two peaks powerful demonstrated the presence of Cd^{2+} [35, 36]. The binding energy spectra for S 2p (Fig. 7c) was resolved into two peaks at 161.6 and 162.7 eV, attributing to S $2p_{3/2}$ and S $2p_{1/2}$ in CdS, respectively [37]. The peak of Ce 3d (Fig. 7b) can be deconvoluted into eight peaks, the peaks of 882.5, 888.9, 898.5 and 901.1, 907.5, 916.9 eV belong to Ce^{4+} , while 885.9 and 903.5 eV belong to Ce^{3+} [38]. As recorded in Fig. 7e O 1s spectral fitting is located at two peaks of 531.4 and 529.0 eV, corresponding to lattice oxygen and chemisorbed oxygen, respectively [39].

3.5 UV–Vis Reflectance Spectrum Analysis

Due to that the optical absorption property is one of the most important factor in determining the photocatalytic performance of semiconductor, the optical properties of CeO_2 , CdS and NR- CeO_2 /CdS composite were investigated using UV–vis DRS, and as recorded in Fig. 8a. The pure NR- CeO_2 sample have the absorption edges of 450 nm, indicating that it has weak visible light absorption. And the CdS shows certain capacity of light absorption with absorption edge at around 500 nm. Compared with pure NR- CeO_2 and CdS, the absorption edge of NR- CeO_2 /CdS exhibits obvious red shift from 450 to 540 nm, indicating that participation CdS to improve the light response effectively. It indicates that the modification with CdS increases the optical absorption. The absorption edge of CeO_2 /CdS shifts significantly in the range of 410 to 550 nm, indicating that the participation of CdS can to improve the light performance effectively. The band gap energy of NR- CeO_2 , CdS derived from Fig. 8b is calculated by the equation, their energy bands can be obtained by underneath formula [40]:

$$\alpha h\nu = A(h\nu - E_g)^{n/2} \quad (1)$$

The α , h and ν represent the absorption coefficient, the Planck constant and the optical frequency while A and E_g are the proportionality constant and the band gap energy, separately [41]. For NR- CeO_2 and CdS, their n values are taken as 2. the E_g of photocatalyst of NR- CeO_2 , and CdS are calculated to be 2.89 and 2.27 eV, respectively, and the calculation results are shown in Fig. 8b. It is easy to find that the bandgap values of these results are close to the reported values [29, 42].

3.6 Photocatalytic Activity

In order to prove that NR- CeO_2 /CdS has better photocatalytic activity, RhB was photodegraded in aqueous solution under simulated sunlight. As shown in Fig. 9a, the degradation rate of RhB reached 94.5% when NR- CeO_2 /CdS(1:1) was irradiated for 3 h. While under the same photocatalytic conditions, the degradation rates of NF- CeO_2 /CdS(1:1), NR- CeO_2 and CdS on RhB were 93.2%, 68.6% and 91.4%, separately. It can be found that NR- CeO_2 /CdS(1:1) has higher photocatalytic activity than pure substance and NF- CeO_2 . The kinetic of pollutant degradation was simulated using the quasi-first-order model, the fitting line are presented in Fig. 9b, NR- CeO_2 , CdS, NR- CeO_2 /CdS(1:1), NF- CeO_2 /CdS(1:1) reaction constant (min^{-1}) were 0.27, 0.72, 0.88, 0.84, separately. NR- CeO_2 /CdS(1:1) reaction rate constants were higher than NR- CeO_2 and CdS 3.26 times and 1.22 times, NR- CeO_2 /CdS(1:1) is 1.05 times of NF- CeO_2 /CdS(1:1). These results further prove that NR- CeO_2 /CdS has higher photocatalytic activity than NF- CeO_2 /CdS. The effect of mass ratio on the photoactivity of samples was also investigated. As shown in Fig. 9c, the mass ratio has a great influence on the photoactivity of the prepared samples. As the ratio of NR- CeO_2 to CdS increased from 1:1 to 1:6, the photoactivity increased gradually. However, with the increase of CdS, the photoactivity decreased significantly.

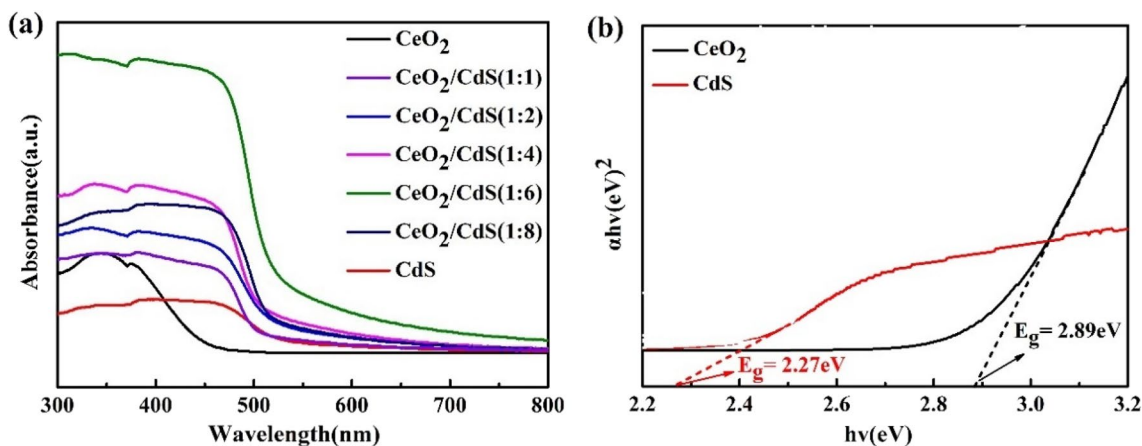


Fig. 8 a UV–Vis DRS of samples; b Tauc plots for the band gap energies originated from UV–Vis DRS

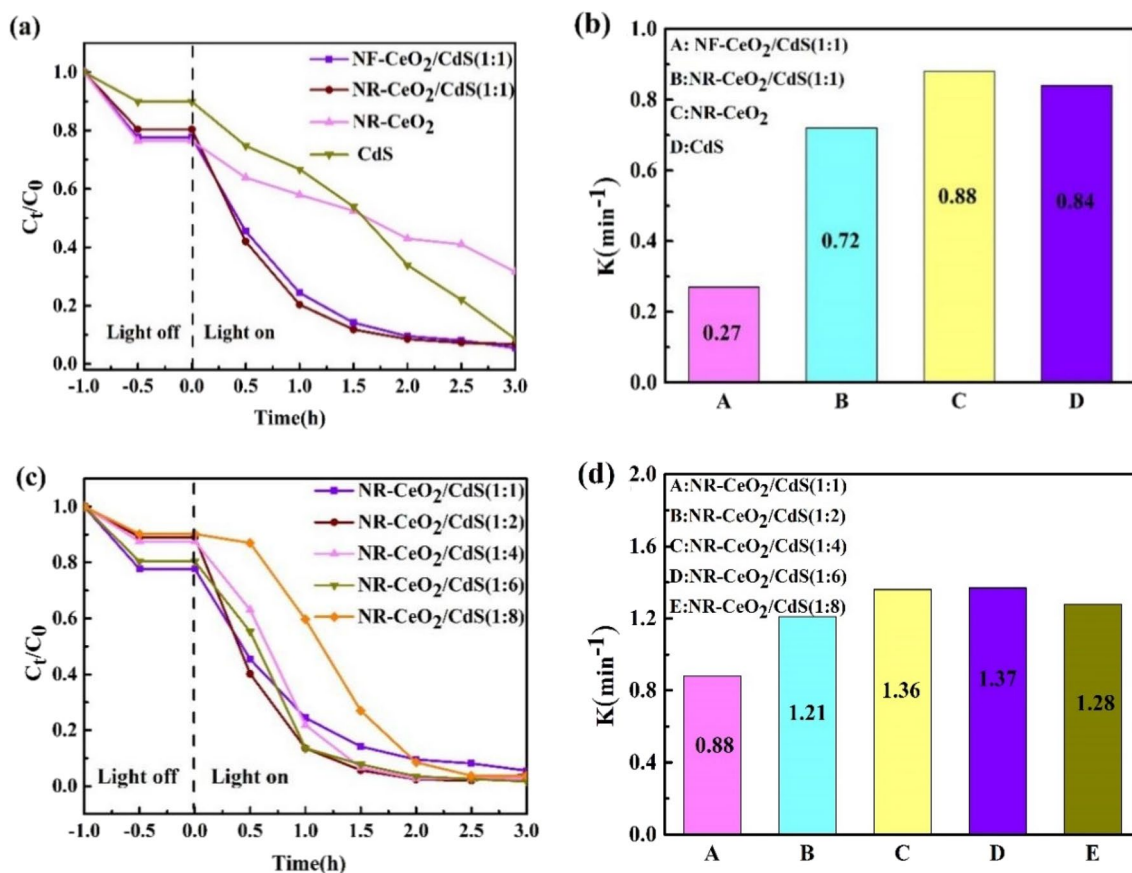


Fig. 9 a Photocatalytic degradation of RhB with different morphologies and pure substances under visible light; b First order kinetic diagram of RhB degradation with different morphologies and pure sub-

stances under visible light; c Photocatalytic degradation of RhB with different proportions under visible light; d First order kinetic diagram of RhB degradation with different proportions under visible light

Therefore, the photoactivity of NR-CeO₂/CdS(1:6) is much higher than that of NR-CeO₂ and CdS. Of course, the reaction rate constant of NR-CeO₂/CdS(1:6) is obviously higher than that of other samples with different proportions in the Fig. 9d.

To demonstrate the stability and reproducibility of the sample, the experiments were repeated on the best sample NR-CeO₂/CdS(1:6). The experimental results showed that, as shown in Fig. 10a, the performance of sample NR-CeO₂/CdS(1:6) remained stable after four cycle experiments. The degradation rates of RhB in the four cycles are 98.3%, 98.2%, 98.0% and 96.1%, respectively. Cyclic experiment results show that NR-CeO₂/CdS(1:6) composite have impressive photocatalytic stability and reusability. Meanwhile, the XRD and SEM results of NR-CeO₂/CdS(1:6) after 4 cycles were compared with those before the cycle. As shown in Fig. 10b and c, NR-CeO₂/CdS(1:6) still maintained high crystallinity after four repeated tests, and the characteristic peak remained unchanged, as well as the morphology. These also manifest that NR-CeO₂/CdS(1:6) had good chemical stability.

3.7 Photoluminescence and Electrochemical Analysis

The photoluminescence (PL) spectroscopy is used to analyze the separation and migration efficiency of photogenerated carriers. Generally, the higher the PL spectrum intensity, the higher the recombination probability of photogenerated carriers. Figure 11a presented the PL spectra of NR-CeO₂, CdS and NR-CeO₂/CdS(1:6) under 280 nm excitation wavelength, the emission peak intensity of NR-CeO₂/CdS(1:6) reduced greatly, demonstrating that the combination of NR-CeO₂ and CdS can inhibit the recombination of photogenerated carriers, and improved electron transfer efficiency, thus making the NR-CeO₂/CdS display an enhanced photocatalytic performance [43]. In order to investigate the migration and separation efficiency of photogenerated electron-hole pairs, I-T of NR-CeO₂, CdS and NR-CeO₂/CdS(1:6) samples was measured. It can be seen from Fig. 11b that the transient photocurrent response of the samples are stable when-on and-off. The photocurrent response of NR-CeO₂/CdS(1:6) under visible light irradiation is significantly enhanced

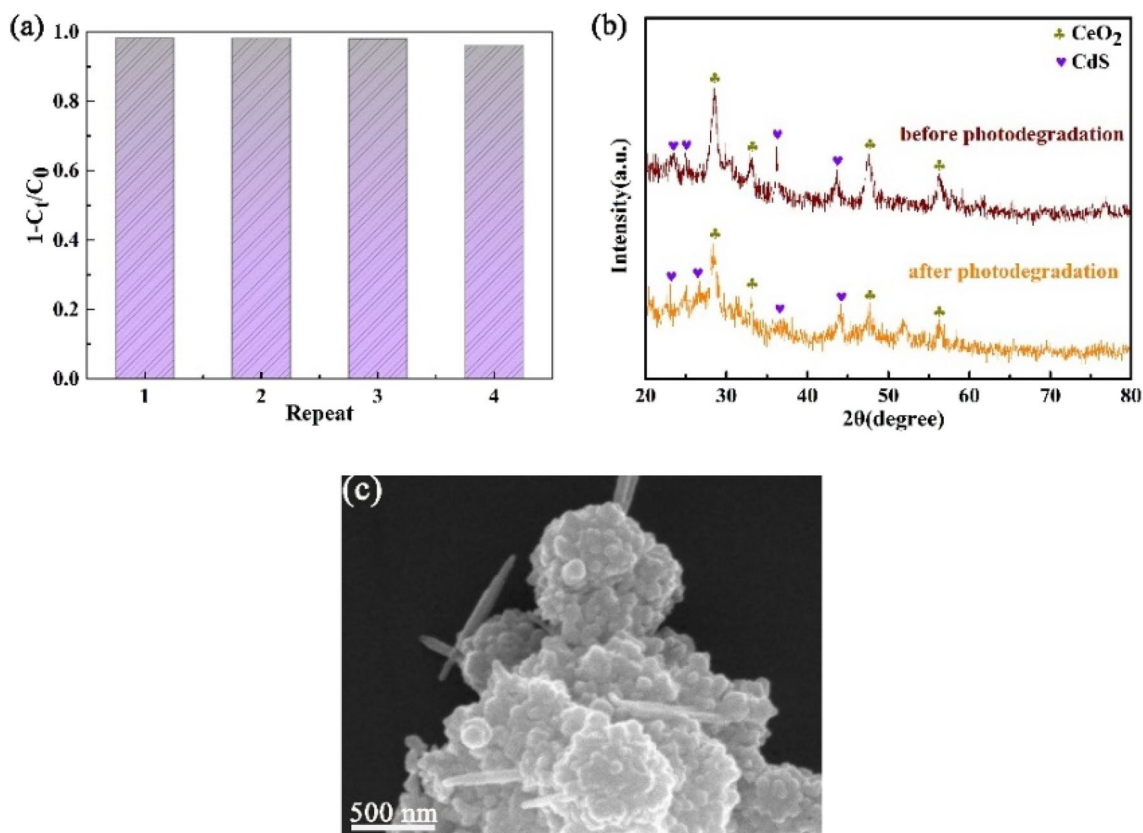


Fig. 10 **a** Cycling experiments of RhB degradation by NR-CeO₂/CdS (1:6); **b** XRD patterns of fresh and used NR-CeO₂/CdS (1:6) (after sixteen cycles); **c** SEM image of NR-CeO₂/CdS (1:6) after cyclic testing

compared with that of pure materials, indicating that the loading of CdS can significantly improve the separation efficiency of photoelectron-hole pairs, thus contributing to the improvement of photocatalytic performance. Figure 11c demonstrates EIS curves of NR-CeO₂, CdS and NR-CeO₂/CdS(1:6). Generally, the electron transfer efficiency is explained by the Radius of Nyquist arc, that is, the smaller the radius of Nyquist arc is, the lower the interfacial charge transfer resistance is. The Nyquist radius of NR-CeO₂/CdS(1:6) composite is the smallest, which indicates the lower electric resistance and higher photo-generated charge separation rate. Therefore, CdS accelerates the transfer and separation of NR-CeO₂ carriers by forming a heterojunction structure. The LSV curves of NR-CeO₂, CdS and NR-CeO₂/CdS(1:6) samples in the Fig. 11d. The overpotential of NR-CeO₂/CdS (1:6) sample is -0.72 V, lower than NR-CeO₂ (-0.75 V). The introduction of CdS improves the ability of electron migration and accelerates the catalytic reaction [44–46], which is consistent with the results of I-T and EIS.

MS curve results of NR-CeO₂, and CdS at 500, 800 and 1000 Hz are shown in Fig. 12. The slope of the fitting curve was positive is n-type semiconductor, so both NR-CeO₂ and CdS are N-type semiconductors, and their flat band

potentials are -1.11 and -1.22 eV (VS Ag/AgCl), respectively. In general, the minimum E_{CB} is 0.1 eV higher than the E_{fb} of n-type semiconductors [47]. Therefore, compared with ordinary hydrogen electrodes, the E_{CB} of NR-CeO₂ and CdS are -1.01 and -1.12 eV, respectively. Their E_{VB} can be converted using formula (2) below:

$$E_{VB} = E_{CB} + E_g \quad (2)$$

Therefore, the E_{VB} values of NR-CeO₂ and CdS are calculated to be 1.88 eV and 1.15 eV, respectively.

3.8 Photocatalytic Mechanism

To analyze the active components formed in the photocatalytic process of NR-CeO₂/CdS(1:6) in Fig. 13a, a free radical capture experiment was carried out. $\cdot\text{OH}$, h^+ and $\cdot\text{O}_2^-$ were captured with IPA, Na₂C₂O₄ and BQ, respectively. Following the addition of 0.1 M BQ into the reaction system, the degradation efficiency of RhB decreased from 98.3% to 10.9%, indicating that $\cdot\text{O}_2^-$ is the key active species in RhB degradation process. Furthermore, after the addition of 0.1 M Na₂C₂O₄ and IPA, the removal efficiency was

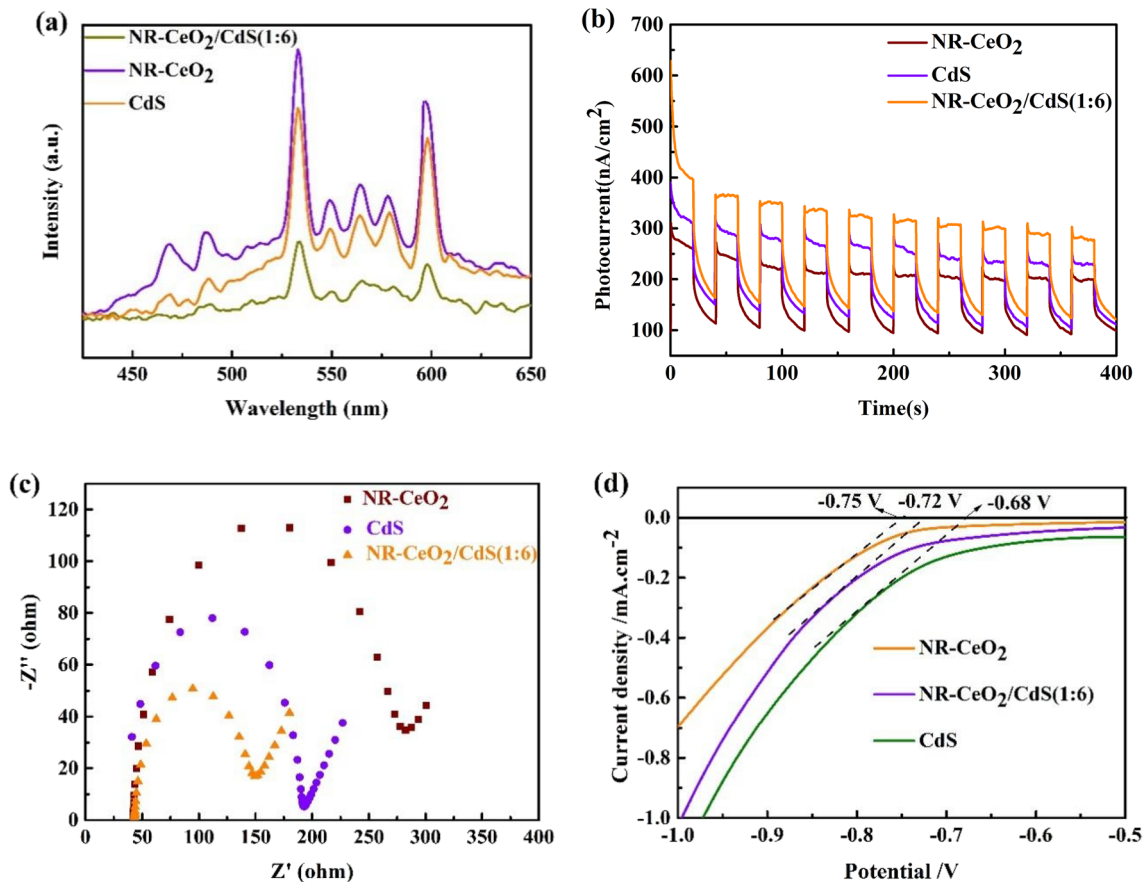


Fig. 11 a PL spectra b Transient photocurrent responses under visible light irradiation c EIS d LSV of NR-CeO₂; CdS and NR-CeO₂/CdS(1:6)

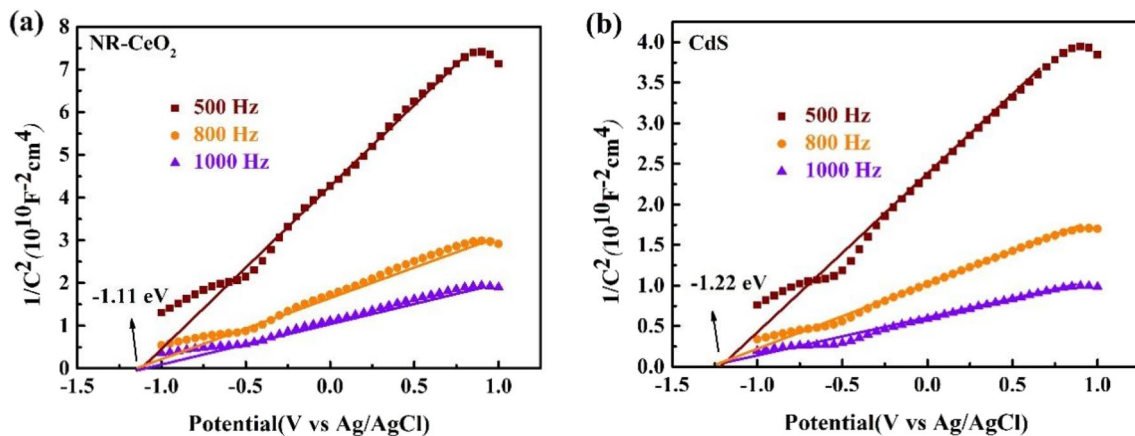


Fig. 12 Mott–Schottky plots of a NR-CeO₂ and b CdS

remained at 59.8% and 80.3%, respectively. In this system, suggesting that h^+ plays the second role in the degradation of RhB. To further detect the active components generated in the NR-CeO₂/CdS(1:6) photocatalytic process, ESR spectroscopy was performed under visible light irradiation and dark conditions, as shown in Fig. 13b and c. Among them,

DMPO as the capture of $\cdot O_2^-$. TEMPO acts as a trap for h^+ [48]. It is observed from Fig. 13b that no signal under dark conditions. However, after 5 min of visible light irradiation, the signal corresponding to $\cdot O_2^-$ is very obvious. In addition, TEMPO-captured ESR spectra of h^+ showed three stable signal peaks in the dark (Fig. 13c). When the visible

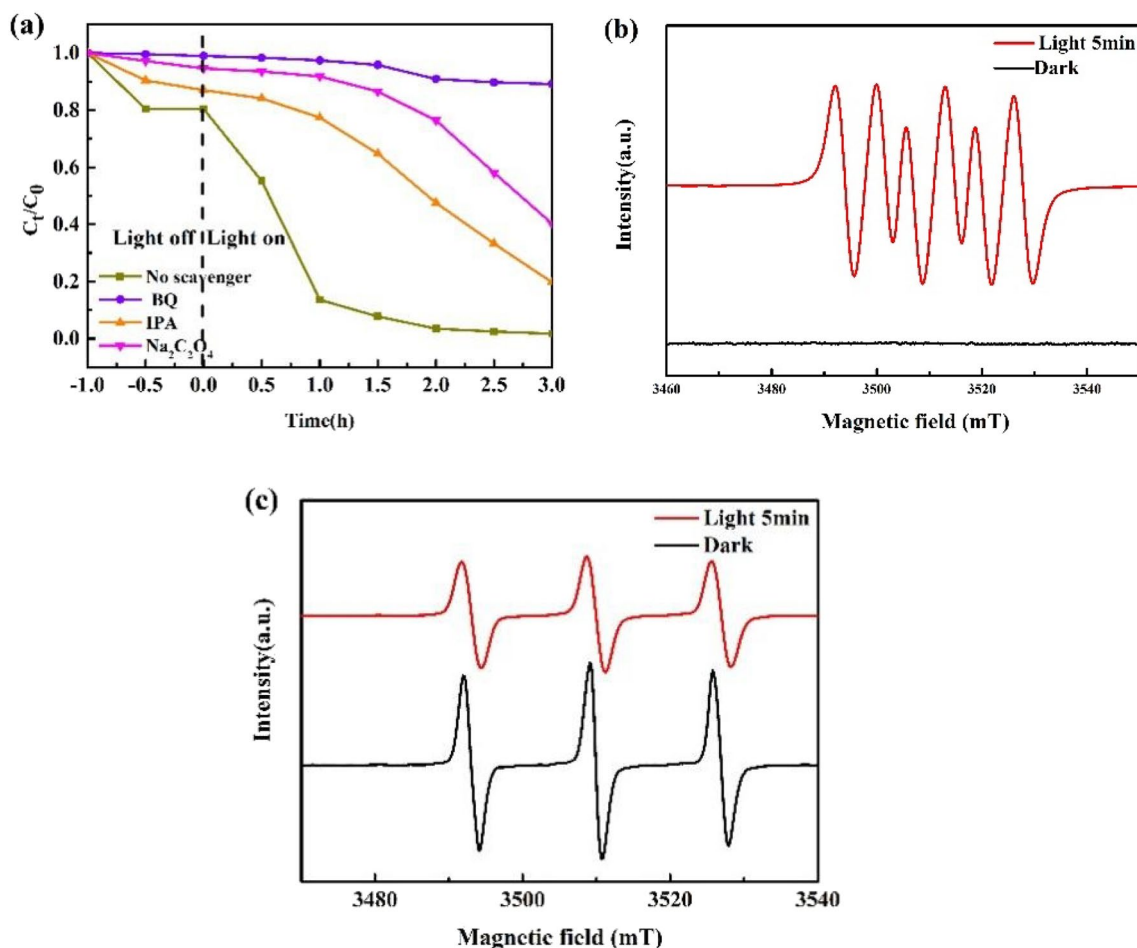


Fig. 13 a Trapping experiment of the active species for the degradation of RhB under visible light irradiation; EPR signals of **b** DMPO-O_2^- ; **(c)** TEMPO-h^+ in the NR-CeO₂/CdS (1:6) under visible light illumination or dark conditions

light was irradiated for 5 min, the signal intensity decreased, which was due to the tempo-induced reaction of photoinduced electrons, oxidized to TEMPO, which indirectly indicated that the generation of h^+ should also contribute to the photocatalytic process [49].

Based on the above experimental data analysis and energy band theory, a possible RhB degradation mechanism is proposed in Fig. 14. Due to the matching of band edge potential, a traditional type II heterostructure is formed between NR-CeO₂ and CdS. When NR-CeO₂ and CdS recombine, the band gap changes and a new Fermi level equilibrium is formed. When exposed to simulated sunlight, the NR-CeO₂/CdS generates holes and photogenerated electrons through photoexcitation. Due to the matching and close contact between NR-CeO₂ and CdS, the photoelectrons accumulated in NR-CeO₂ ($E_{\text{CB}} = -1.12$ eV) of CdS migrate to CB ($E_{\text{CB}} = -1.01$ eV) of NR-CeO₂. However, the holes will transfer from the VB of NR-CeO₂ ($E_{\text{VB}} = 1.88$ eV) to the VB of CdS ($E_{\text{VB}} = 1.15$ eV) [49]. The electrons on CB of NR-CeO₂ will be captured by O₂ to generate $\cdot\text{O}_2^-$. As a reactive oxygen species, $\cdot\text{O}_2^-$ can oxidize

RhB into degradation products. In addition, holes accumulated on CdS can interact directly with RhB. According to the transferring circulation of h^+/e^- , the internal electric field was established between NR-CeO₂ and CdS to inhibit the recombination of h^+ and e^- pairs, thus improving the photodegradation efficiency. Under solar simulated irradiation, the reaction process of NR-CeO₂/CdS can be expressed by the following formula:

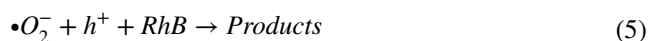
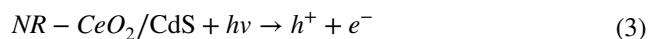
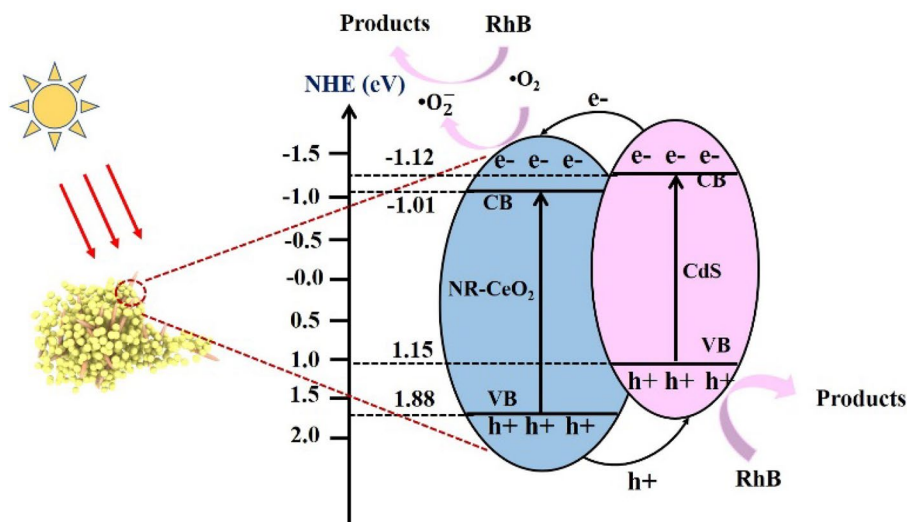


Fig. 14 Schematic diagram of photocatalytic mechanism for RhB degradation over NR-CeO₂/CdS



4 Conclusion

In summary, a series of CeO₂/CdS photocatalysts were prepared using cerium nitrate as precursor by a facile solvothermal method and assisted calcination method. The effects of the morphology, composite proportion and preparation technology on the photocatalytic activity of the composites were investigated, and the degradation mechanism of the composites was also discussed. The results showed that the composite effect of NR-CeO₂/CdS was better than that of NF-CeO₂/CdS, and the degradation efficiency of NR-CeO₂/CdS (1:6) was as high as 98.3%, which was much higher than that of CdS and NR-CeO₂. This may be because different crystal planes exposed of CeO₂ lead to different degradation properties. Furthermore, NR-CeO₂/CdS (1:6) showed good stability after four RhB photodegradation cycles. To determine the reasons for the excellent photocatalytic performance of NR-CeO₂/CdS (1:6), a large number of experiments and characterization analyses were carried out. SEM, TEM and UV–Vis DRS show that NR-CeO₂/CdS (1:6) has a 3D rod-like heterojunction structure and good optical properties. XPS, UV–Vis DRS, electrochemical analysis show that the Schottky junction formed at the NR-CeO₂/CdS interface is beneficial to the high separation and transfer efficiency of photogenerated carriers. This study provides an effective method and theoretical basis for interface and surface design of composite catalysts. Finally, free radical trapping experiments and ESR demonstrated the involvement of active species (h⁺ and •O₂⁻), and verified the type II transfer mechanism of NR-CeO₂/CdS composite. Therefore, this work not only provides an effective method for catalyst interface design to prepare catalysts with high photodegradation rate and good reusability, but also has potential applications in the treatment of organic dyes.

Author contributions ZL: Writing—Original draft preparation; YZ: Reviewing and Editing; Funding acquisition; LD: Project Administration, Resources; Formal analysis; HM: Reviewing and Editing, Formal analysis; DL: Validation, Data curation; LW: Data curation; ST: Investigation.

Funding This research was supported by the National Natural Science Foundation of China (NSFC, 52105332).

Declarations

Conflict of interest The authors declare that they have no known competing financial interests or personal relationships that could have appeared to influence the work reported in this paper.

References

1. M. Ren, Y. Ao, P. Wang, C. Wang, *Chem. Eng. J.* **378**, 122122 (2019)
2. J. Zhang, J. Fang, X. Ye, Z. Guo, Y. Liu, Q. Song, S. Zheng, X. Chen, S. Wang, S. Yang, *Appl. Surf. Sci.* **480**, 557–564 (2019)
3. H. Wang, Y. Wu, M. Feng, W. Tu, T. Xiao, T. Xiong, H. Ang, X. Yuan, J.W. Chew, *Water Res.* **144**, 215–225 (2018)
4. S. Chakrabarti, B.K. Dutta, *J. Hazard. Mater.* **112**, 269–278 (2004)
5. W. Zhang, G. Li, H. Liu, J. Chen, S. Ma, M. Wen, J. Kong, T. An, *Appl. Catal. B: Environ.* **272**, 118969 (2020)
6. K. Qi, W. Lv, I. Khan, S.Y. Liu, *Chin. J. Catal.* **41**, 114–121 (2020). [https://doi.org/10.1016/S1872-2067\(19\)63459-5](https://doi.org/10.1016/S1872-2067(19)63459-5)
7. U.G. Akpan, B.H. Hameed, *J. Hazard. Mater.* **170**, 520–529 (2009)
8. A. El Golli, M. Fendrich, N. Bazzanella, C. Dridi, A. Miotello, M. Orlandi, *J. Environ. Manag.* **286**, 112226–112226 (2021)
9. P. Gao, J. Liu, D.D. Sun, W. Ng, *J. Hazard. Mater.* **250**, 412–420 (2013)
10. M. Aslam, M.T. Qamar, M.T. Soomro, I.M.I. Ismail, N. Salah, T. Almeelbi, M.A. Gondal, A. Hameed, *Appl. Catal. B* **180**, 391–402 (2016)
11. T. Montini, M. Melchionna, M. Monai, P. Fornasiero, *Chem. Rev.* **116**, 5987–6041 (2016)
12. E.M. Seftel, M.C. Puscasu, M. Mertens, P. Cool, G. Carja, *Appl. Catal., B* **150**, 157–166 (2014)

13. E.M. Seftel, M.C. Puscasu, M. Mertens, P. Cool, G. Carja, *Appl. Catal., B* **164**, 251–260 (2015)
14. R. Ma, S. Zhang, T. Wen, P. Gu, L. Li, G. Zhao, F. Niu, Q. Huang, Z. Tang, X. Wang, *Catal. Today* **335**, 20–30 (2019)
15. Z.M. Yang, G.F. Huang, W.Q. Huang, J.M. Wei, X.G. Yan, Y.Y. Liu, C. Jiao, Z. Wan, A. Pan, *J. Mater. Chem. A* **2**(6), 1750–1756 (2014)
16. S. Hu, F. Zhou, L. Wang, J. Zhang **12**(9), 794–797 (2011)
17. Y. Ma, Y. Bian, Y. Liu, A. Zhu, H. Wu, H. Cui, D. Chu, J. Pan, *ACS Sustain. Chem. Eng.* **14**, 134–146 (2022)
18. C. Li, R. Chen, X. Zhang, S. Shu, J. Xiong, Y. Zheng, W. Dong, *Mater. Lett.* **65**(9), 1327–1330 (2011)
19. J. Low, J. Yu, M. Jaroniec, S. Wageh, A.A. and Al-Ghamdi, *Adv. Mater.* **29**, 1601694 (2017)
20. J. Tian, Y. Sang, Z. Zhao, W. Zhou, D. Wang, X. Kang, H. Liu, J. Wang, S. Chen, H. Cai, H. Huang, *Small* **9**, 3864–3872 (2013)
21. Y. Zhang, Q. Shao, H. Jiang, L. Liu, M. Wu, J. Lin, J. Zhang, S. Wu, M. Dong, Z. Guo, *Inorg. Chem. Front.* **7**(6), 1345–1361 (2020)
22. L. Cheng, Q. Xiang, Y. Liao, H. Zhang, *Energy Environ. Sci.* **11**, 1362–1391 (2018)
23. C. Xue, H. An, G. Yang, *Catal. Today* **317**, 99–107 (2018)
24. D. You, B. Pan, F. Jiang, Y. Zhou, W. Su, *Appl. Surf. Sci.* **363**, 154–160 (2016)
25. Z. Li, J. Zhang, J. Lv, L. Lu, C. Liang, K. Dai, *J. Alloy. Compd.* **758**, 162–170 (2018)
26. M. Madkour, A.A. Ali, A. Abdel Nazeer, F. Al Sagheer, C. Belver, *Appl. Surf. Sci.* **499**, 143988 (2020)
27. J. Yu, Y. Yu, P. Zhou, W. Xiao, B. Cheng, *Appl. Catal. B* **156**, 184–191 (2014)
28. Q. Gao, Y. Cui, H. Zhang, S. Wang, B. Liu, C. Liu, *Sep. Purif. Technol.* **274**, 119116 (2021)
29. J. Yao, Z. Gao, Q. Meng, G. He, H. Chen, *J. Colloid Interf. Sci.* **594**, 621–634 (2021)
30. J. Ren, Y. Zheng, K. Yuan, L. Zhou, K. Wu, Y. Zhang, *Nanoscale* **12**, 755–762 (2020)
31. M. Schwarz, F. Faisal, S. Mohr, C. Hohner, K. Werner, T. Xu, T. Skála, N. Tsud, K.C. Prince, V. Matolín, Y. Lykhach, *J. Phys. Chem. Lett.* **9**, 2763–2769 (2018)
32. W. Chen, B. Han, C. Tian, X. Liu, S. Liang, H. Deng, Z. Lin, *Appl. Catal. B* **244**, 996–1003 (2019)
33. L. Zhou, S. Cao, L. Zhang, G. Xiang, J. Wang, X. Zeng, J. Chen, Facet effect of Co₃O₄ nanocatalysts on the catalytic decomposition of ammonium perchlorate. *J. Hazard. Mater.* **392**, 122358–122365 (2020)
34. X. Zhou, Z. Liu, Y. Wang, Y. Ding, Facet effect of Co₃O₄ nanocrystals on visible-light driven water oxidation. *Appl. Catal. B* **237**, 74–84 (2018)
35. Q. Cai, Z. Hu, Q. Zhang, B. Li, Z. Shen, *Appl. Surf. Sci.* **403**, 151–158 (2017)
36. R. Chen, P. Wang, J. Chen, C. Wang, Y. Ao, *Appl. Surf. Sci.* **473**, 11–19 (2019)
37. Z. Wu, X. Yuan, G. Zeng, L. Jiang, H. Zhong, Y. Xie, H. Wang, X. Chen, H. Wang, *Appl. Catal. B-Environ.* **240**, 373–379 (2019)
38. S.W. Lv, J.M. Liu, N. Zhao, C.Y. Li, F.E. Yang, Z.H. Wang, S. Wang, *Sep. Purif. Technol.* **253**, 117413 (2020)
39. X. Hu, H. Zhao, Y. Liang, R. Chen, *Appl. Catal. B* **258**, 117966 (2019)
40. J. Zhu, Y. Shen, X. Yu, J. Guo, Y. Zhu, Y. Zhang, *J. Alloy. Compd.* **771**, 309–316 (2019)
41. J. Ding, Z. Dai, F. Qin, H. Zhao, S. Zhao, R. Chen, *Appl. Catal. B* **205**, 281–291 (2017)
42. X. Ruan, H. Hu, H. Che, E. Jiang, X. Zhang, Chunbo Liu, G. Che, *J. Colloid Interf. Sci.* **543**, 317–327 (2019)
43. Y. Li, L. Ding, Z. Liang, Y. Xue, H. Cui, J. Tian, *Chem. Eng. J.* **383**, 123178 (2020)
44. Z.Y. Li, Q.L. Zhang, L.K. Wang, J.Y. Yang, Y. Wu, Y.M. He, *Adv. Powder Technol.* **80**, 105795 (2021)
45. X. Xu, L. Xiao, Z. Wu, Y. Jia, X. Ye, F. Wang, B. Yuan, Y. Yu, H. Huang, G. Zou, *Nano Energy* **78**, 105351 (2020)
46. L.L. Cheng, D.Y. Huang, Y. Zhang, Y. Wu, *Adv. Powder Technol.* **32**(9), 3346–3354 (2021)
47. W. Zhen, X. Ning, B. Yang, Y. Wu, Z. Li, G. Lu, *Appl. Catal. B- Environ.* **221**, 243–257 (2018)
48. D.D. Peng, Y. Zhang, G. Xu, Y. Tian, D. Ma, Y. Zhang, P. Qiu, *A.C.S. Sustain. Chem. Eng.* **8**, 6622–6633 (2020)
49. F. Chen, Q. Yang, Y. Zhong, H. An, J. Zhao, T. Xie, Q. Xu, X. Li, D. Wang, G. Zeng, *Water Res.* **101**, 555–563 (2016)

Publisher's Note Springer Nature remains neutral with regard to jurisdictional claims in published maps and institutional affiliations.

Springer Nature or its licensor (e.g. a society or other partner) holds exclusive rights to this article under a publishing agreement with the author(s) or other rightsholder(s); author self-archiving of the accepted manuscript version of this article is solely governed by the terms of such publishing agreement and applicable law.